

Characteristic Time Scales of Reservoir Evaporation in a Subarctic Climate

Adrien Pierre¹, Daniel Nadeau¹, Antoine Thiboult¹, Alain N. Rousseau², Alain Tremblay³, Pierre-Erik Isabelle¹, and François Anctil¹

¹Université Laval Département de Génie Civil et de Génie des Eaux

²INRS Eau Terre Environnement

³Hydro-Quebec

February 22, 2024

Abstract

Water bodies such as lakes and reservoirs affect the regional climate by acting as heat sinks and sources through the evaporation of substantial quantities of water over several months of the year. Unfortunately, energy exchange observations between inland water bodies and the atmosphere remain rare in northeastern North America, which has one of the highest densities of lakes in the world. This study helps to fill this gap by analyzing field observations collected from a subarctic hydropower reservoir (50.69°N, 63.24°W) characterized by a mean depth of 44 m and a surface area of 85 km². Two eddy covariance (EC) systems, one on a raft and one onshore, were deployed from 27 June 2018 to 12 June 2022. The thermal regime of the reservoir was monitored using vertical chains of thermistors. Results indicate a mean annual evaporation rate of 590 ± 66 mm (~70% of the annual precipitation), with 84% of the evaporation occurring at a high rate from August to freeze-up in late December through episodic pulses. It was difficult to close the energy balance because of the magnitude and the large time lag of the heat storage term. In order to circumvent this problem, we opted to perform calculations for a year that started from the first of March, as the heat storage in the water column was at its lowest at that point and could thus be ignored. From June to December, monthly Bowen ratios increased from near-zero negative values to about 1.5. After September, due to smaller vapor pressure deficits, latent heat fluxes steadily declined until an ice cover sealed up the reservoir. Two opposite diurnal cycles of sensible and latent heat fluxes were revealed during the open water period, with sensible heat fluxes peaking at night and latent heat fluxes peaking in the afternoon.

1. INTRODUCTION

Reservoirs are subject to substantial water level fluctuations caused by water release operations and, as such, to shorter water residence times than lakes. Evaporation (latent heat flux, LE) is a major component of the mass and energy budgets of reservoirs, which can compromise some typical key functions such as freshwater supply, irrigation, hydropower, navigation, and other related economic activities (Friedrich et al., 2018). In some arid regions of the world, structural measures are put in place to limit evaporation, such as floating balls or lattices (Assouline & Narkis, 2021). Evaporation is intangible and therefore a difficult hydrological flux to measure, making it difficult to fully understand its magnitude and controlling mechanisms.

Studies that have quantified reservoir evaporation are rare. Tanny et al. (2008) reported an average evaporation rate of 5.5 mm day⁻¹ from July to September in the Eshkol reservoir in Israel (33°N), which has a hot and arid climate. Further north, in the Eastmain-1 reservoir in Canada (52°N), Strachan et al. (2016) found the evaporation rate to be 3.1 mm day⁻¹ between August and October. For the Great Slave Lake in Canada (61°N), Rouse et al. (2003) reported 2 mm day⁻¹ in summer and 5 mm day⁻¹ in December. These studies indicate that even in cold regions, reservoir evaporation can be substantial.

In cold climates, reservoirs undergo two turnovers per year (dimictic). Their thermal regime typically evolves into three successive phases (Cole & Weihe, 2016). During the ice cover phase, ice acts as a lid over the water body, preventing direct interactions between the atmosphere and the water column. The water column then becomes stratified, with cold water ($< 4\text{degC}$) sitting on top of warmer water. Latent heat fluxes tend to remain low during this period (Wang et al., 2016). From ice breakup in spring to the middle or end of summer, the heat storage phase unfolds. Energy is first stored in the top several meters of the water column closer to the surface and eventually reaches deeper layers due to wind-induced mixing and internal hydrodynamics (Spence et al., 2003; Vincent, 2018). The result is a surface mixing layer (epilimnion) that is separated from the homogeneous deep layer (hypolimnion) by a zone with a steep temperature gradient (metalimnion). Latent heat fluxes remain low during this phase, with frequent and stable atmospheric stratification. The third and final phase corresponds to the heat release period. This is characterized by a decline in water temperature due to a substantial release of energy into the atmosphere through turbulent heat fluxes that are high and sustained day and night (Blanken et al., 2011). The epilimnion then slowly deepens until the fall turnover, during which the temperature of the entire water column becomes homogenous.

While evaporation varies seasonally in response to the three thermal phases, it also fluctuates on smaller time scales in response to meteorological forcing. For instance, incoming shortwave radiation causes latent heat fluxes to peak during the day, thereby increasing the rate of evaporation during peak times (Lensky et al., 2018). The atmospheric demand for water vapour, driven by wind speed and vapour pressure deficit, is also known to modulate evaporation in water bodies (Perez et al., 2020). Evaporative demand can vary within a single day. For instance, changing wind direction can lead to a reduced or enhanced sheltering effect, increasing or decreasing evaporation rates (Markfort et al., 2010; Venalainen et al., 1998). Evaporation can also vary over the course of a few days, due to passing synoptic systems that can generate sustained evaporation (Laird & Kristovich, 2002; Spence et al., 2013). Blanken et al. (2000) found that 50% of annual evaporation over the Great Slave Lake occurred over only 25% of the year through episodic evaporation water losses. Moreover, thermocline depth and intensity, which depends in part on the reservoir morphometry (Gorham, 1964), influence turbulent heat fluxes by limiting or enhancing the energy available in the upper water layers. Indeed, Piccolroaz et al. (2015) identified positive feedback between the lake surface temperature and the stratification dynamics of Lake Superior, Canada. Therefore, the timing of evaporation occurs at different scales and remains poorly documented or correlated to physical drivers (Beck et al., 2018).

Northeastern America is one of the densest regions of lakes and reservoirs around the world (Downing et al., 2006). These lakes and reservoirs are considered to be climate sentinels (Adrian et al., 2009; Williamson, Saros, & Schindler, 2009) as well as integrators and regulators of climate change (Williamson, Saros, Vincent, et al., 2009). Wang et al. (2018) showed that modifications in surface energy allocation under warmer climate conditions will accelerate global lake evaporation. In-situ evaporation observations are needed to develop and improve lake models (McJannet et al., 2017) for future climate estimates, particularly in remote areas.

There is a lack of direct in-situ measurements of turbulent heat fluxes over reservoirs in remote northern regions. The overarching goal of this study is to identify the characteristic time scales of evaporation from a deep subarctic hydropower reservoir. Using four years of eddy-covariance (EC) measurements, the specific objectives are to quantify turbulent heat fluxes at daily, monthly and annual time scales, and to identify the key processes and surface energy budget terms that govern LE at each time scale. The paper is organized as follows. We first introduce the study site and measurement methods. Then, we describe the meteorological conditions over the whole study period and the driving factors for each time scale. Finally, uncertainties in the flux data are discussed, given the energy budget of several water layers in the reservoir.

2. MATERIALS AND METHODS

2.1 Study Site

The study site is located at the southern tip of the Romaine-2 hydropower reservoir, 80 km north of the city of Havre-Saint-Pierre, on the north shore of the Gulf of St. Lawrence, Quebec, Canada (50.68degN , 63.25degW ; Fig. 1a). The Romaine-2 reservoir is a dimictic water body that is ice-free from May to

December. The regional climate has a mean annual air temperature and precipitation of 1degC and 852 mm (52% as rain), respectively (Hydro-Quebec, 2007). This is typical of the subarctic (Dfc) Koppen-Geiger climate classification type (Beck et al., 2018). The reservoir, which flooded in 2014, drains a 14,351-km² area that is mostly covered with a spruce-moss forest. At its southern end, the reservoir is about 1 km-wide, and sits at an elevation of 244 m above mean sea level. When full, it has a surface area of 85.6 km² and a maximum depth of 101 m (mean depth of 44 m). It has an elongated north-south shape that channels the near-surface winds. Hydropower production imposes large water level fluctuations, up to 17 m in winter and 2 m in summer and fall (Fig. 2a), resulting in a smaller surface area during these seasons when the water is shallow. Turbine flow rates also fluctuate yearly, with maximum values in winter when the demand for energy is at its maximum (Fig. 2b) and during freshet to avoid spillage. The study period extended from 27 June 2018 to 12 June 2022.

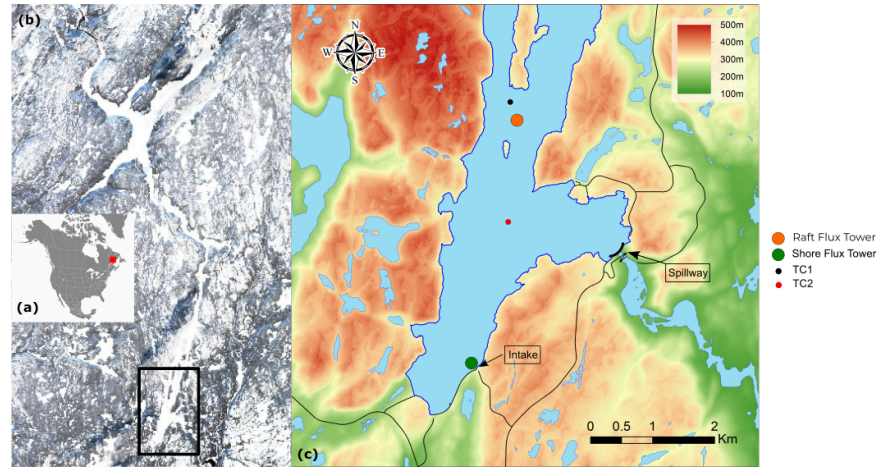


Figure 1: (a) Location of the Romaine-2 reservoir in North America (red square). (b) Satellite image (Sentinel-2A, 2022-01-26) of the Romaine-2 reservoir in winter. The black rectangle indicates the area of the experimental setup (c). (c) Elevation map indicating precisely where the spillway, intake, flux towers and thermistor chains (indicated by TC) are located.

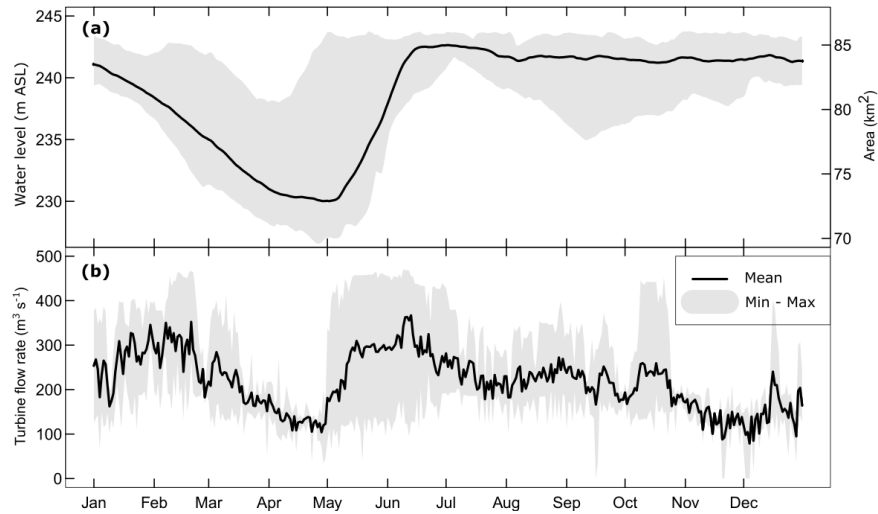


Figure 2: (a) Romaine-2 daily water levels (Above Sea Level) and (b) turbine outflow rate. Both plots

feature the average (black solid line) and the full range of observed values (grey shaded area) for the 2018 to 2021 period. No data were collected in 2022.

2.2 Raft and Shore Flux Tower

Figure 3 shows the two flux towers that were deployed on the research site: a 3×3 -m raft (measurement height of 2.0 m) deployed from June to October each year and a permanent shore tower (measurement height fluctuating between 11 and 28 m depending on the water level) (Fournier et al., 2021; Pierre et al., 2022). At both sites, the eddy covariance technique was used to calculate turbulent heat fluxes from raw 10-Hz turbulence data.

The raft was anchored between two islands to offer protection against large waves, in a 30-m deep section of the reservoir. The raft hosted a fast-response sonic anemometer coupled with an infrared gas analyzer (IR-GASON, Campbell Scientific, USA), a net radiometer (Kipp & Zonen, The Netherlands) and a temperature probe, all mounted 2 m above the water surface. Turbulence sensors were oriented eastward to capture the prevailing wind directions while minimizing flow distortion by the mast. The raft slowly oscillated along its three Euler angle axis due to wave-induced motions. To decontaminate raw wind measurements, an accelerometer (AHRS, Lord Sensing MicroStrain, USA) was attached adjacent to the anemometer to record pitch, yaw, and roll angles at a frequency of 10 Hz.

At the shore site, the flux tower was equipped with a combined sonic anemometer and infrared gas analyzer (IRGASON, Campbell Scientific, USA), installed 11 m above the maximum water level and pointing toward the reservoir in the NNW direction. A complete meteorological setup was also deployed: a TB4 tipping bucket (Hyquest Solutions, USA) for rainfall measurement, a propeller anemometer (05103, R.M.Young, USA), and a four-component net radiometer (CNR4, Kipp & Zonen, The Netherlands). The last two instruments were installed at heights of 10.3 m and 12.3 m, respectively. The radiometer measured all terms of the radiation budget, namely incoming and outgoing shortwave and longwave radiation, but since the instrument was installed on the shore, it did not report the radiation emitted/reflected by the reservoir.

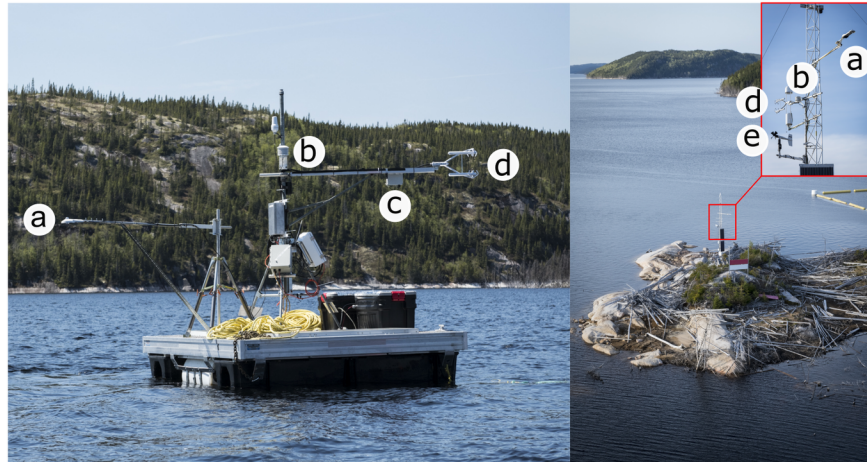


Figure 3: The two eddy covariance measurement setups deployed on and around the Romaine-2 reservoir. Raft station (left, photo taken looking west) and shore station (right, photo taken looking north) with the following instruments: (a) net radiometer, (b) air temperature probe, (c) accelerometer, (d) sonic anemometer and infrared gas analyzer, and (e) propeller anemometer. Photos were provided by Hydro-Québec and taken on 13 June 2019, at approximately 2 m below the maximum reservoir level.

A complete year-long net radiation time series was created using the following strategy. We used the net radiation that was measured on the raft when it was deployed (June-October). When ice was present on the reservoir, it was typically covered in snow. We therefore assumed that the emitted/reflected radiation

measured at the shore station during that time was equivalent to what would have been measured on the reservoir. During the transition periods, we estimated the reflected radiation on the reservoir with a simple albedo formula based on that by Patel and Rix (2019). The longwave radiation emitted during the transition periods was estimated from the Stefan-Boltzmann law. This was done by taking an emissivity of 0.995 and extrapolating the water temperature profile in the top first meter of water to estimate the water skin temperature for periods when no direct measurements were available.

2.3 Turbulent Heat Fluxes

Sensible (H) and latent heat fluxes (LE) (both in W m^{-2}) were calculated using the covariance between the vertical wind speed w (m s^{-1}) and air temperature T (K), as well as between w and the specific humidity q (kg kg^{-1}), such that:

$$H = \rho_a c_{pa} w' T' \quad (1)$$

$$LE = \lambda \rho_a w' q' \quad (2)$$

where ρ_a is the humid air density (kg m^{-3}), c_{pa} is the specific heat of humid air ($\text{J kg}^{-1} \text{K}^{-1}$) and λ is the latent heat of vaporization (J kg^{-1}). Here, primes denote fluctuations from the 30-min average, indicated by an overbar.

Raw wind velocity data from the raft were first corrected for wave-induced motion, using the accelerometer data, following the method proposed by Miller et al. (2008). In short, the apparent wind measured by the sonic anemometer was corrected to account for Euler angles, angular velocities and linear accelerations monitored by the accelerometer. Then, for the shore and raft flux towers, we processed the turbulence data using the EddyPro® software, version 7.0 (LI-COR Biosciences, USA). In doing so, we applied time-lag compensation, linear detrending, double rotation approach (Baldocchi et al., 1988; Wilczak et al., 2001), density fluctuation compensation (Webb et al., 1980), spike removal (Papale et al., 2006), and other statistical tests (Vickers & Mahrt, 1997). Poor-quality data were flagged (Mauder & Foken, 2011) and removed. Data from the raft and shore stations were aggregated into one dataset by favoring data with the best quality criteria (Mauder et al., 2013). Note that shore data were retained only when winds originated from the reservoir. To complete the final dataset, gap-filling was implemented based on the method developed by Reichstein et al. (2005).

Over the whole study period (1447 days), 57 % of the turbulent flux data had to be gap-filled due to the fact that the raft was only deployed from June to October and the shore flux tower was frequently exposed to winds from the surrounding land. We assessed flux errors by applying the Finkelstein and Sims (2001) random uncertainty method.

2.4 Water Temperature and Transparency

The vertical water temperature profile was continuously measured with two chains of temperature probes (HOBO TidBit UTBI-001, Onset, USA) that were designed with a higher resolution near the surface and a coarser resolution deeper in the water (Figs 3c and 4). These are referred to as thermistor chains (TCs). The first measurement site, TC_1 , consisted of a 15-m chain deployed in a 30-m deep section of the reservoir, in the vicinity of the raft. The second measurement site, TC_2 , consisted of a 70-m chain located in a 100-m deep section of the reservoir, 1 km south of the raft. At both sites, skin temperatures were obtained using floating sensors sheltered from incoming solar radiation by a white piece of foam. The chains were designed to withstand variations in water levels by using additional rope. A pressure sensor (HOBO water level logger u20-001-03, Onset, USA) was added to each chain to correct for the effects of rope tilt on the exact vertical position of the probes.

Water transparency was also periodically measured using a Secchi disc. The mean Secchi depth (SD) was 4 ± 0.04 m. Assuming a mean product $SD \times K_d$ of 2.28 for water of moderate transparency following Koenings

and Edmundson (1991), the vertical attenuation coefficient K_d becomes 0.57 m^{-1} . Consequently, 50% of the incident energy flux density is absorbed in the first 1.2 m of water and 99% over the first 8.1 m of water.

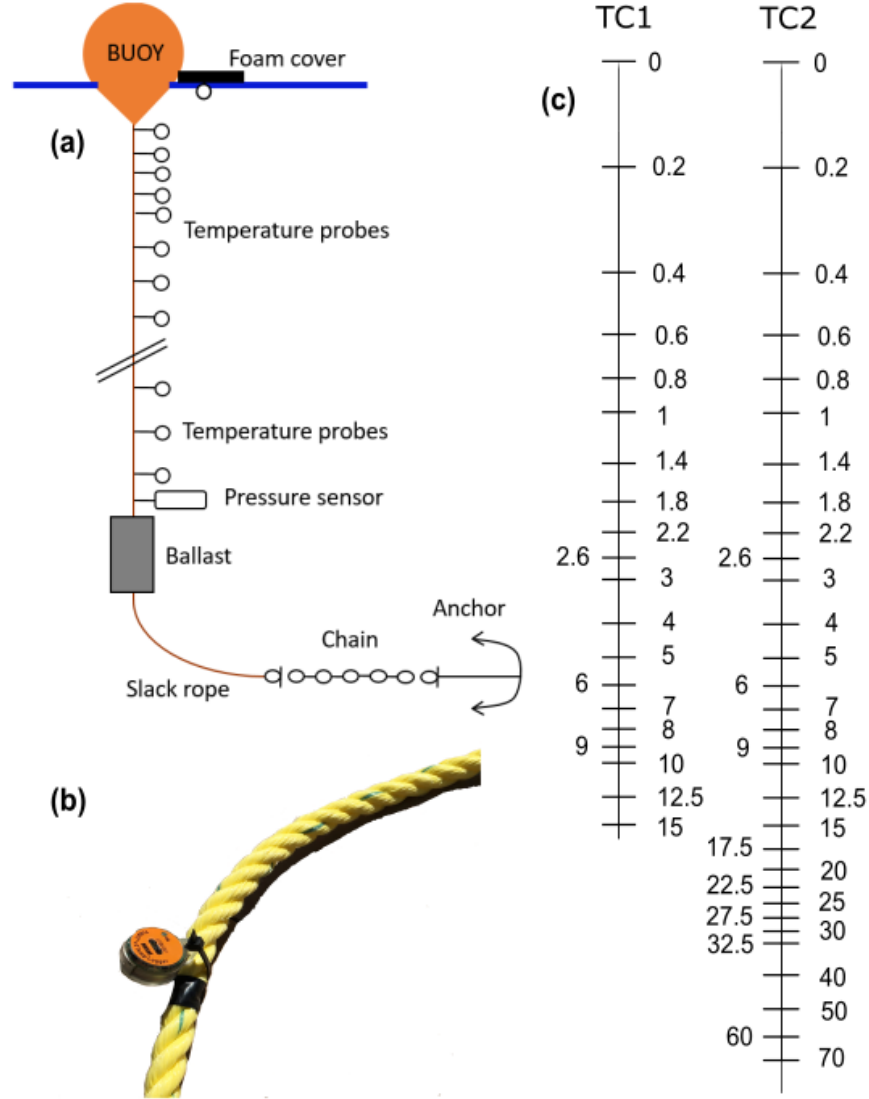


Figure 4: (a) Schematic of the thermistor chain (TC) components, (b) TidBit temperature probes (HOBO TidBit UTBO-001, Onset, USA) installed on the chains, and (c) the resolution of temperature measurements presented on a logarithmic scale (in m).

2.5 Energy Balance Ratio

The energy balance ratio (Feng et al., 2016) allows us to quantify the energy balance closure and therefore to correct underestimated turbulent heat fluxes (see Sect. 3.3). It is defined as follows:

$$\text{EBR} = \frac{H + LE}{R_n - H_S} \times 100 \quad (3)$$

where R_n is the net radiation and ΔH_S is the heat storage variation along the water column, defined as

$$H_S = \int_0^h \rho_w c_{pw} \frac{T_w}{t} dh \quad (4)$$

where ρ_w is the water density (kg m^{-3}), c_{pw} is the specific heat of water ($\text{J kg}^{-1} \text{K}^{-1}$), ΔT_w is the water temperature difference between two time steps (K), Δt is the time period (30 min), and h is the water layer thickness (m). To determine the EBR, ΔH_S was calculated over the entire depth of the epilimnion, which is the distance between the surface (0 m) and the position of the thermocline (h). Note that the epilimnion thickness varies over the year. On average, $h = 15$ m from June to October, $h = 30$ m from November to December, and $h = 0$ m from January to May.

2.6 Ice Cover

Ice cover was monitored using a time-lapse camera (Reconyx, Holmen, WI, USA) that took hourly photos of the southern edge of the reservoir. Water temperatures were also used to identify the solar radiation penetration into the water column and as such, ice formation, as ice and snow cover reduce or prevent radiation from entering the water column.

Figure 5 illustrates the key phases of the reservoir regime. The ice-free period (Fig. 5a) and the ice-cover period (Fig. 5c) are separated by the onset (Fig. 5b) and break-up (Fig. 5d) of ice.

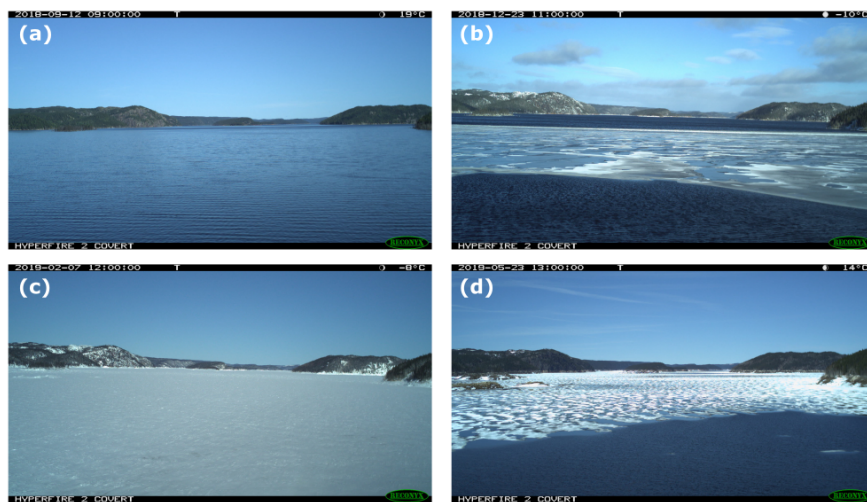


Figure 5: Photographs (looking north) illustrating some key phases of the reservoir regime: (a) open-water period (12 September 2018), (b) start of freeze-up (23 December 2018), (c) full ice and snow cover (7 February 2019), and (d) ice breakup (23 May 2019).

3. RESULTS & DISCUSSION

3.1 Meteorological Conditions

The overall meteorological conditions observed over the Romaine-2 reservoir were typical of a subarctic climate (Fig. 6), with cool and humid summers along with cold and dry winters. Wind speed (WS) was generally quite high, particularly in the fall and winter when daily averages occasionally reached 15 m s^{-1} , but showed a marked decline in summer. The reservoir was mostly colder than the air above it between May and July (the heat storage period). The vapour pressure deficit (VPD) values were high from mid-spring to mid-autumn.

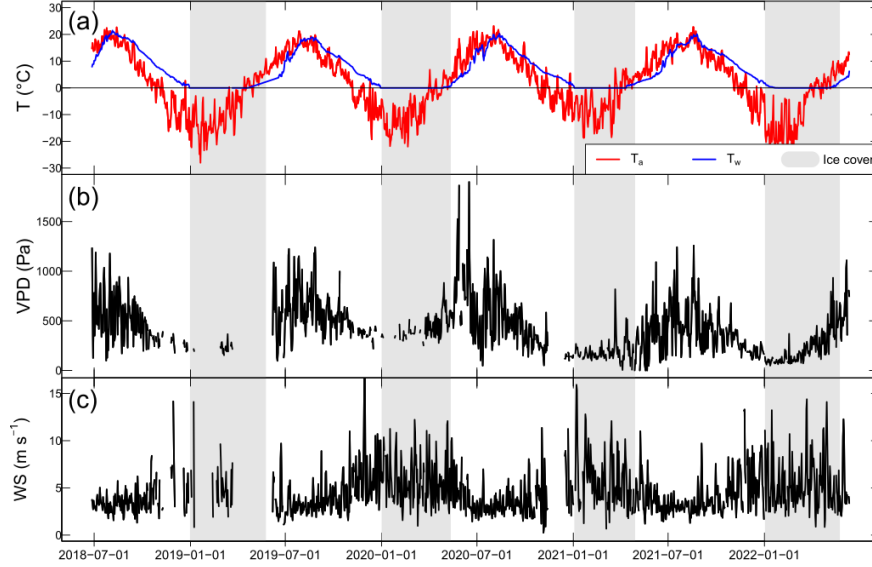


Figure 6: Daily means of (a) 2-m air (T_a) and near-surface water temperatures (T_w), (b) vapor pressure deficit (VPD), and (c) wind speeds (WS) collected at the raft and shore sites. The period with ice cover (shaded area) was determined from time-lapse photos.

The distribution of the wind direction measured from the raft flux tower followed a bimodal pattern, aligned along the SSW-NNE axis of the reservoir. Wind measured from the reservoir at the shore flux tower showed the same pattern. The 30-min mean wind speed was 5.6 m s^{-1} while the maximum wind speed reached 19.4 m s^{-1} .

3.2 Heat Fluxes

3.2.1 Daily Scale

Figure 7 illustrates the average diurnal cycles of H and LE during ice cover (January to mid-May), the heat storage phase (mid-May to August), and heat release (September to December). The last two phases are defined based on the heat storage curve presented in Figure 13. The 70-m heat storage peaked in early September, marking a transition from the storage period to the release period. In fact, it is important to note that the storage and release phases of the reservoir overlap during August, as heat release starts in early August while heat storage continues to grow in the water column until early September.

During the ice cover periods, LE remained low ($< 20 \text{ W m}^{-2}$) and positive, which is indicative of sublimation, while H was negative ($< -10 \text{ W m}^{-2}$). Both turbulent heat fluxes had diurnal cycles with an amplitude lower than 10 W m^{-2} . The corresponding Bowen ratios were small and negative when LE was between 5 W m^{-2} and 10 W m^{-2} . These results were expected, as ice and snow covered the water surface from early January until mid-May, suggesting low albedo and preventing the surface from heating up enough to produce stronger turbulent heat fluxes.

From mid-May to August, LE values remained low, with an average of nearly 30 W m^{-2} and a maximum of up to 60 W m^{-2} at 14:00. H then showed a clear diurnal cycle, at -30 W m^{-2} at 15:00 and close to 0 W m^{-2} at night. A value of -60 W m^{-2} was reached in early afternoon. As a result, the Bowen ratio also exhibited a diurnal cycle.

During the heat release phase (September to December), LE remained larger than H at all times, meaning that energy was mainly released through phase change (evaporation). One striking feature is that LE and H had opposite daily patterns: (i) LE reached a maximum at around 15:00 while H reached a minimum, and (ii) LE reached a minimum at 00:00 while H peaked at 5:00. LE peaked in the afternoon when the incident

solar radiation reached its maximum value, warming up the water surface during the day. Maximum H values occurred at night, when the maximum water-air temperature difference was observed. At a similar temporal scale, Nordbo et al. (2011) observed fluxes over the small, boreal Lake Valkea-Kotinen in Finland and showed that the highest values of LE and H occurred in June, peaking at 15:00 and at 06:00 respectively. Therefore, in this study, the Bowen ratio exhibited an explicit diurnal cycle. The highest values were around 0.95 at night because of high H and low LE values. The lowest values were around 0.40 in the day because of low H and high LE values. As a result, heat was released by two different mechanisms depending on the time of the day: through both turbulent heat fluxes at night and mainly through evaporation during the day. Overall, the sensible heat fluxes H contributed to the heat stored by the water body early in summer, that will later be released as latent heat flux.

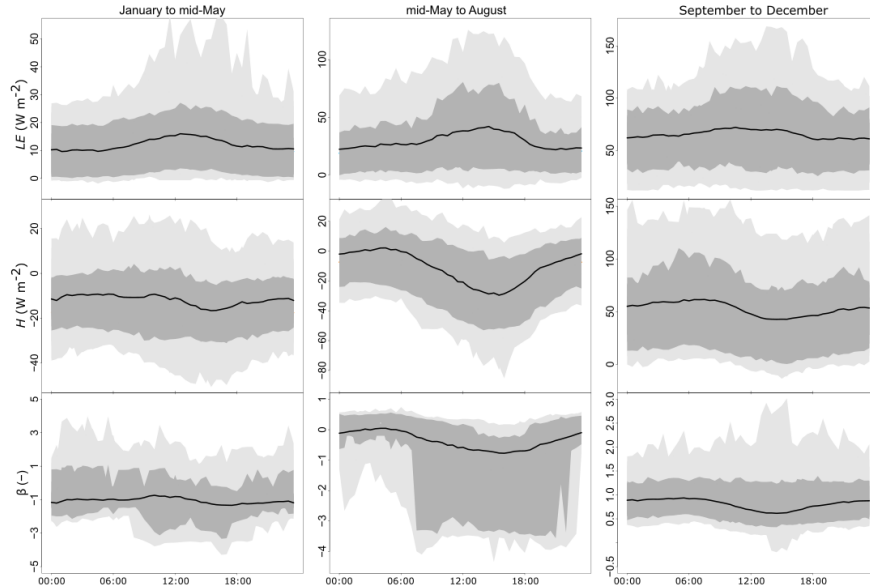


Figure 7: Average diurnal cycle of (top) latent heat flux, (middle) sensible heat flux, and (bottom) Bowen ratios, with the interquartile (dark shading) and the 10 to 90 quantile zones (light shading). The left column are data for January to mid-May (ice cover), the central column covers mid-May to August (heat storage), and the right column covers September to December (heat release). Note that the range of the ordinate values varies from one plot to the other. All times are local.

Condensation episodes ($LE < 0 \text{ W m}^{-2}$) occurred occasionally throughout the study period. During winters, small and short condensation episodes occurred almost every day. However, during the vernal turnover, conditions became very stable and the atmosphere was much warmer than the water surface, which was nearly constant at 4°C . Consequently, only a few condensation events were recorded between 1 May and 17 July, with cumulative amounts of 2.2 mm, 0.6 mm and 3.4 mm in 2019, 2020 and 2021, respectively. Figure 8 presents examples of condensation events that occurred in June, temporarily reaching -10 W m^{-2} or 0.35 mm day^{-1} .

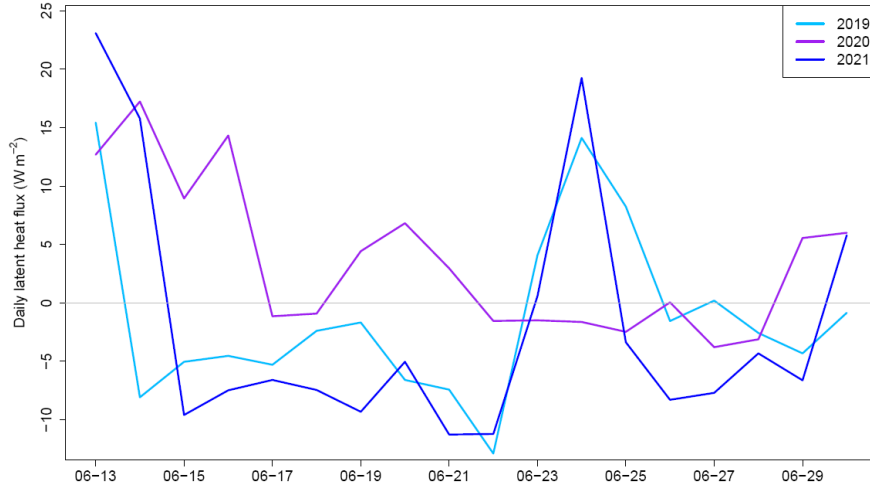


Figure 8: Daily mean latent heat flux for 2019 (light blue), 2020 (purple) and 2021 (blue), illustrating the occurrence of condensation episodes between 13 and 30 June.

The reservoir was exposed to many episodes of sustained evaporation, defined as consecutive 24-h periods with a daily mean $LE \geq 100 \text{ W m}^{-2}$ (i.e., daily mean $LE \geq 3.5 \text{ mm}$), ranging from one to several days. Of those, the most modest episode caused 3.5 mm of evaporation in one day (obviously), while the largest episode caused 29.3 mm of evaporation in 6 days ($\approx 5 \text{ mm day}^{-1}$). Figure 9 presents the number of sustained evaporation events for each month and their durations. Most events were of short duration but had high evaporation rates: 80% of events lasted 2 days or less. The mean rate of evaporation was 0.2 mm h^{-1} for all events. As a comparison, Blanken et al. (2011) reported that most of the evaporation from Lake Superior occurred in 2.5- to 3-day episodic pulses.

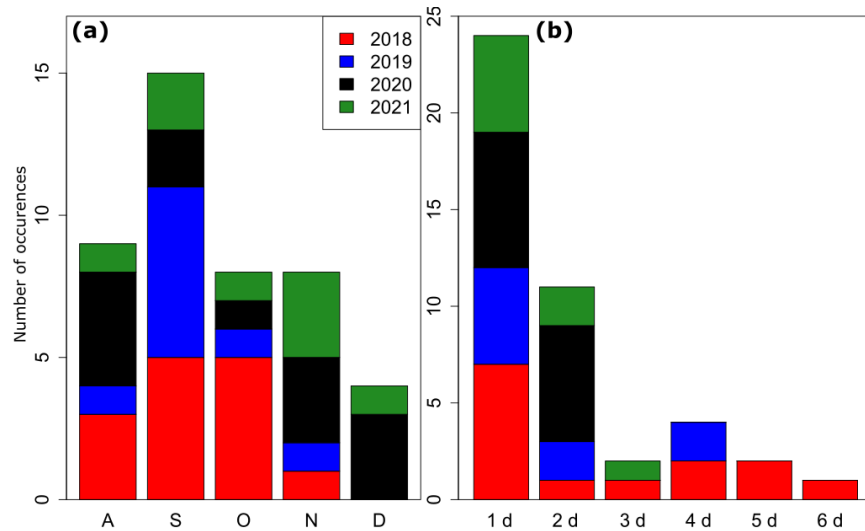


Figure 9: Sustained evaporation events, defined as consecutive days with at least 3.5 mm of daily evaporation. (a) Number of occurrences per month: A (August), S (September), O (October), N (November), D (December); and (b) number of occurrences for different durations.

Figure 10 presents several variable time series during two strong evaporative events. These episodes occur when air becomes drier (decline of at least 50% of the specific humidity) in conjunction with high wind

speeds. This may be due to the passage of a low pressure system (Figure 10, left) or a high pressure system (Figure 10, right).

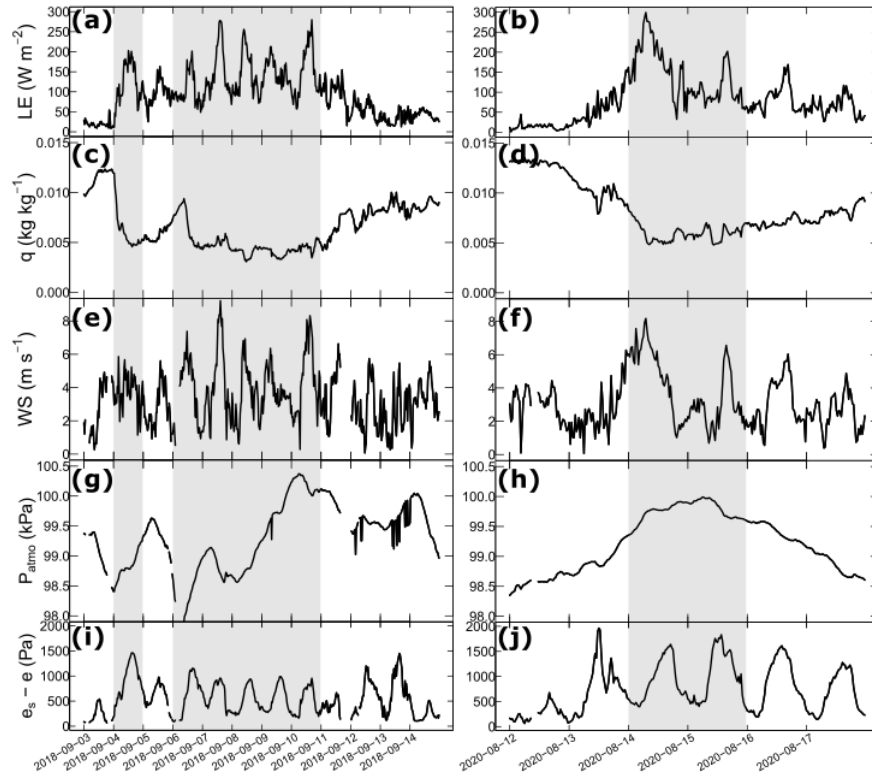


Figure 10: Three sustained evaporation episodes (left, 1-day and 5-day episodes in September 2018, and right, 2-day episode in August 2020) with 30-min time series of (a, b) latent heat fluxes, (c, d) specific humidity, (e, f) wind speed, (g, h) atmospheric pressure, and (i, j) vapor pressure deficit. Shaded zones indicate high evaporation events.

3.2.2 Monthly Scale

Figure 11 displays monthly averaged turbulent heat fluxes over the whole study period. Latent heat fluxes always remained positive despite some condensation events in June (Sect. 3.2.1). LE peaked in September, when the heat storage reached its maximum (Fig. 13). It remained above 70 W m^{-2} from August to October. LE began to rise in July when stratification in the reservoir set in. It then sharply increased in August all the way to December, during which 84% of the annual evaporation occurred. This is consistent with the findings from Blanken et al. (2011) for Lake Superior, where 89% of the annual evaporation occurred when there was unstable atmospheric stratification. It is also consistent with the Rouse et al. (2003) study at Great Slave Lake, where 85% to 90% of evaporation occurred during a period when the atmosphere was unstable. However, in our study, LE decreased gradually due to the declining vapour pressure deficit that followed the decline in air temperature. In winter and spring, LE stayed below 20 W m^{-2} and reached its minimum in June, during the ice-free period (Fig. 6).

Sensible heat fluxes were negative from February to July, with values less than -10 W m^{-2} and reaching as low as -20 W m^{-2} when the reservoir was colder than the air. On average, values remained positive from August to January. In June, the reservoir was ice-free while the water column was under vernal transition, with upper layers that were not warm enough to stratify (i.e., below 3.98°C , the temperature of maximum water density). The water surface temperature stayed far below the air temperature, preventing H from

becoming positive and enabling LE to become negative. Despite the high net radiation term around the summer solstice, the heat content of the water body only slowly rose because of the high specific heat and density of water. In summer and fall, the surface layers were warmer than the air above the water. H increased steadily until December, reaching 80 W m^{-2} , and then decreased abruptly in January as the water surface froze. From May to August, net radiation (R_n) was high, contributing mostly to the storage of heat in the reservoir (ΔH_S), while turbulent heat fluxes were relatively low. Nearly all the energy brought in by R_n was used to increase the heat storage term. During the fall and early winter, R_n declined rapidly while LE and H increased, fuelled by the energy stored in the reservoir, firmly establishing the heat release period of the reservoir. We observed a three-month delay between the maximum summer net radiation that occurred in June and the maximum latent heat flux. The delay was six months between the peak net radiation and the maximum sensible heat flux. We also observed different delays between the maximum surface water temperature and the maximum LE and H , which were delayed by one and four months, respectively.

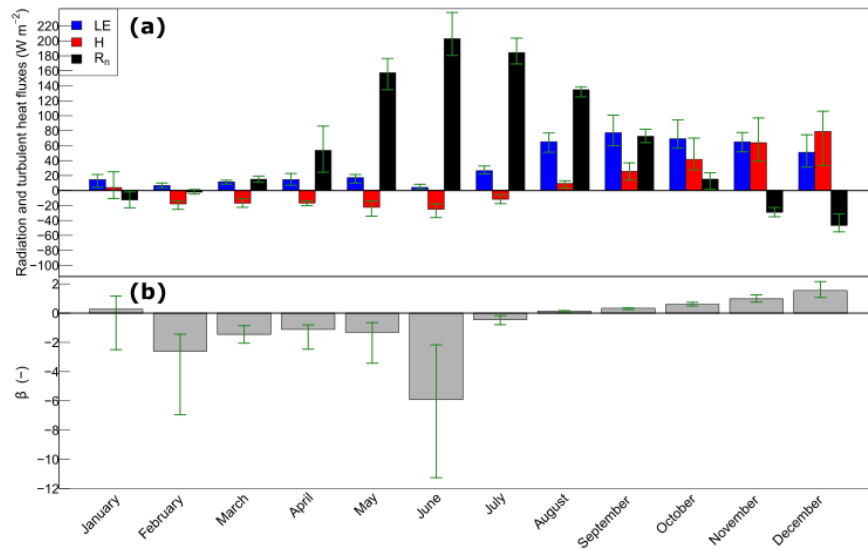


Figure 11: (a) Monthly sensible heat flux (red), latent heat flux (blue) and net radiation (black) from June 2018 to December 2021. Bars indicate monthly minimum and maximum average values. (b) Monthly Bowen ratio. The error bars indicate the maximum and minimum values observed for each month.

The Bowen ratios exhibited high negative values during the first seven months of each year due to low LE values. After the onset of the heat release period (end of July), it stayed around zero before gradually increasing to about 1.5 in December. This indicates that the reservoir was mostly releasing heat through sensible heat flux, as evaporation was constrained by the small vapour pressure deficit induced by the cold air temperatures.

The energy state of the reservoir is closely tied to the stability regime of the overlying atmosphere. During heat release (August to early January), the overlying atmosphere was unstable, while it remained mostly stable during the heat storage (mid-May to August) and ice-cover periods. Figure 12 explores the relationship between daily LE and atmospheric stability ζ for heat storage and release. The figure confirms that larger daily evaporation occurs under near-neutral ($\zeta \approx 0$) and unstable conditions ($\zeta < 0$), and that stable conditions ($\zeta > 0$) are related to low evaporation rates. Note that condensation occurred primarily under near-neutral and stable conditions.

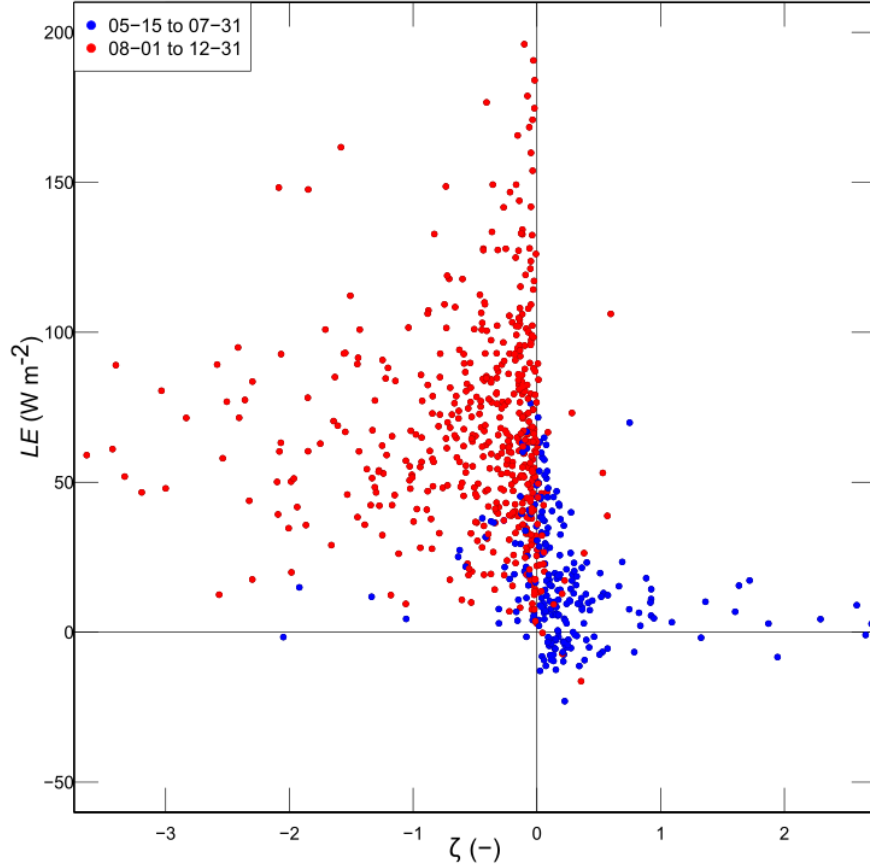


Figure 12: Daily latent heat flux as a function of atmospheric stability ($\zeta = \frac{z}{L_{Ob}}$ where z is the measured height and L_{Ob} refers to the Obukhov length) for the ice-free periods (15 May to 31 December) from 2018 to 2021.

Figure 13 presents the 2018, 2020 and 2021 cumulative heat storage ΔH_S calculated over the 70-m water column. Heat storage started in spring and ended in early September (a 3.5-month period), with maximum values of 2000 $MJ m^{-2}$ for 2018 and 2021 and 1700 $MJ m^{-2}$ for 2020. Heat release followed and lasted about 4 months until ice-on. The heat release rate was lower from September to mid-November compared to mid-November to the end of December: 13 $MJ m^{-2} day^{-1}$ compared to 21.7 $MJ m^{-2} day^{-1}$ for 2018. Overall, heat storage exhibited larger day-to-day fluctuations than heat release.

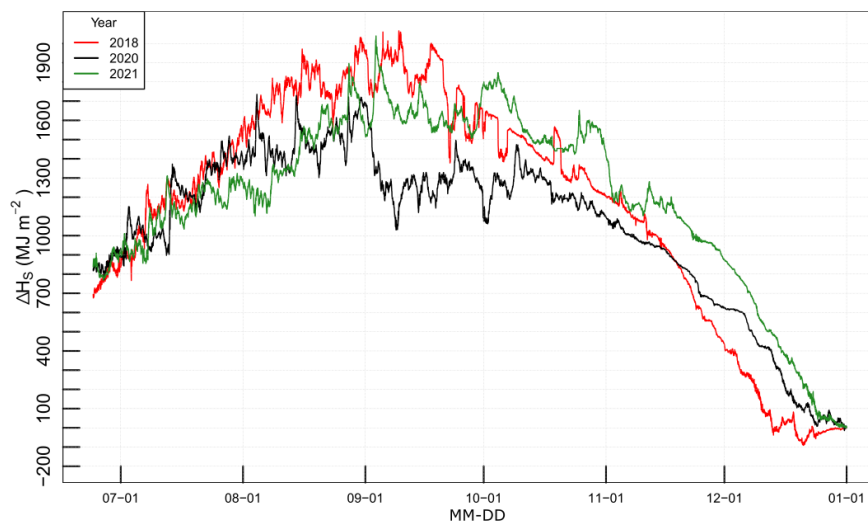


Figure 13: Cumulative heat storage in the upper 70 m of the water column for years 2018, 2020 and 2021. There are no data shown for 2019 due to a major thermistor chain malfunction. Calculations start from 24 June as no data were recorded before this date for 2018 and 2020. For the purposes of the figure, to create a reference point based on our data availability, we set the annual cumulative heat storage at the end of the year to zero ($\Delta H_S = 0 \text{ MJ m}^{-2}$).

Note that Romaine-2 experienced a sharp drop in heat storage in September 2020. This is linked to the approximately 10 m decline in water level in August and September. Indeed, the epilimnion moved closer to the water intake and therefore the accumulated heat within the top layers was drained out as turbine flow. The year 2020 was therefore unusual in terms of heat storage.

When looking at the monthly layer energy balance of the reservoir using equation 3, we noted that there was a significant non-closure. This is due to the time scale difference between the heat storage in the water column and the remaining terms (turbulent heat fluxes and net radiation). Indeed, due to the high thermal inertia and the high specific heat of water, the net radiation that was received in summer accumulated in the water column and was only released in autumn. This feature makes it difficult to calculate the EBR on a monthly scale. Within this context, correcting turbulent heat fluxes to account for the energy imbalance (Foken, 2008) using the monthly EBR is problematic, unless accurate measurements of lateral energy inputs are available (sect. 3.3).

3.2.3 Annual Scale

Calculating annual reservoir evaporation values is challenging. It is well understood that eddy covariance data underestimate turbulent heat fluxes (Foken, 2008), and in addition, the calculation of the heat storage term is especially difficult for a deep water column. For this reason, an alternative approach was used: the corrected turbulent heat fluxes were obtained by redistributing the missing energy according to the annual EBR over a so-called "energy year," from March 1 to February 28 of the next year. Since energy storage is typically at its minimum value at this time of year, this allowed us to discard that variable and make $R_n = H + LE$. Since $R_n > H + LE$, the missing energy can then be redistributed by preserving the observed Bowen ratio, as discussed in Mauder et al. (2018). By doing so, the EBR was 80%, 69%, and 76% for the years 2019-20, 2020-21, and 2021-22, respectively.

Figure 14 illustrates the yearly cumulative evaporation for three energy years, from 2019 to 2022. The mean annual non-corrected evaporation was $439 \pm 23 \text{ mm}$ and did not vary much from year to year. When correcting for the energy imbalance using the annual EBR values, the annual evaporation values reached 555 mm, 656 mm and 559 mm for 2019-20, 2020-21 and 2021-22, respectively (refer to Table 1). Note that

the inter-annual variabilities of cumulative evaporation were 7.2% and 18% for non-corrected and corrected values, respectively. In fact, 50% of the total measured evaporation occurred over 24%, 27% and 26% of the days for 2019-20, 2020-21 and 2021-22, respectively. This is consistent with Blanken et al. (2000), who found a mean value of 22.5% for the Great Slave Lake.

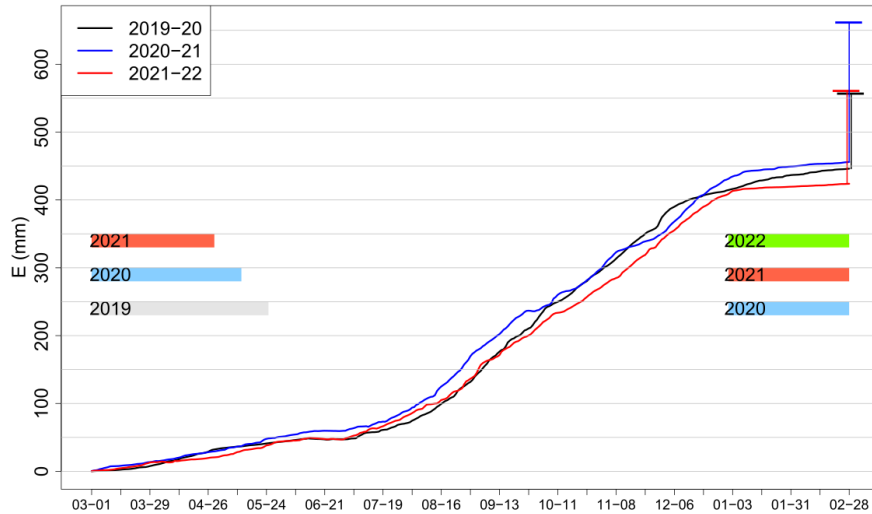


Figure 14: Cumulative annual evaporation from 1 March to 28/29 February of the following year, for 2019-20, 2020-21 and 2021-22. Pale green, red, blue and grey bars represent the duration of the respective ice cover periods. Horizontal bars at the end of the energy period represent corrected annual evaporation, compensating for the lack of closure of the energy balance based on the annual EBR (see Table 1).

Few studies have focused on annual scales of lake or reservoir evaporation in the boreal biome. In Canada, Strachan et al. (2016) reported that the evaporation rate at the Eastmain-1 reservoir was 595 mm yr^{-1} , reaching $100 \text{ mm month}^{-1}$ in summer and 3.1 mm d^{-1} from August to October. Rouse et al. (2003) found the annual evaporation at Great Slave Lake to be between 384 mm and 506 mm yr^{-1} and daily evaporation ranged from 2 mm d^{-1} in summer to 5 mm d^{-1} in December. For Lake Tåmnaren in Sweden, Heikinheimo et al. (1999) reported 281 mm of evaporation from May to October. Finally, Blanken et al. (2011) found the annual evaporation at Lake Superior to be up to 645 mm . However, it is important to note that these studies were all based on eddy-covariance measurements and did not take into consideration the non-closure of the energy balance, meaning that they did not correct for cumulative evaporation values. This appears to be one major shortcoming in the annual estimation of turbulent heat fluxes.

Table 1 presents important meteorological characteristics for each year of the study period. Note that 2020 experienced the lowest turbine volume in the study, probably due to the upstream flooding of the Romaine-4 reservoir, which might explain the slightly higher evaporation. The highest temperature anomaly by a fair margin occurred in 2021, while wind speed anomalies remained low and constant throughout the study period.

Table 1: Annual characteristics from 2018 to 2021. Non-corrected and corrected total of evaporation, ice cover period, turbine outflow volume, temperature and wind speed anomalies compared to 1991-2020 (ERA5 values) and total net radiation.

Years	2018 - 19	2019 - 20	2020 - 21	2021 - 22
Non-corrected total evaporation (mm)	-	446	456	423
Corrected annual evaporation (mm) see Sect. 3.3	-	555	656	559
Ice cover period (days)	-	145	133	119

Years	2018 - 19	2019 - 20	2020 - 21	2021 - 22
Turbine outflow volume (km ³)	6.1	7.4	5.6	8.5
Temperature anomaly (°C)	-0.4	-0.4	+0.7	+3.5
Wind speed anomaly (m s ⁻¹)	+0.01	+0.2	+0.03	+0.03
Total net radiation (MJ m ⁻²)	-	1844	2046	1970

When examining the inter-annual variation of cumulative evaporation, we noted that the seasonal onset and the break-up of ice cover did not have a large impact on total yearly evaporative losses. The longer ice cover period in 2019 (145 days) than that of 2020 (133 days) resulted in lower cumulative evaporation. This trend is not repeated in 2021, which featured the shortest ice cover period (119 days) and lower cumulative evaporation compared to 2020 (Fig. 14). We also noted that the timing of ice onset was very consistent, as it began around January 1 of each year, while ice break-up was more variable between years. As for duration, the onset of ice lasted between two and three weeks while ice break-up lasted five to seven weeks prior to the reservoir becoming completely ice-free.

3.3 Uncertainties

There are uncertainties that affected the EC measurements that were used in this study. Random sampling uncertainties were calculated following Finkelstein and Sims (2001) and amounted to [?] 2% for both sensible and latent heat fluxes over the whole study period. In addition, the error associated with gap-filling was noteworthy for H , LE and R_n because of the difficulty of measuring fluxes over an inland water body. The use of a raft results in oscillations that must be considered in the calculation process, while the use of a flux tower on the shore limits the measurement period over the reservoir.

EC measurements were also subject to underestimations linked to the lack of energy balance closure (Foken, 2008), which is best described in terms of the energy balance ratio (EBR, equation 3). Figure 15 illustrates the monthly EBR values in the reservoir for 2019 to 2021. This confirms that the energy budget layer was subject to non-closure.

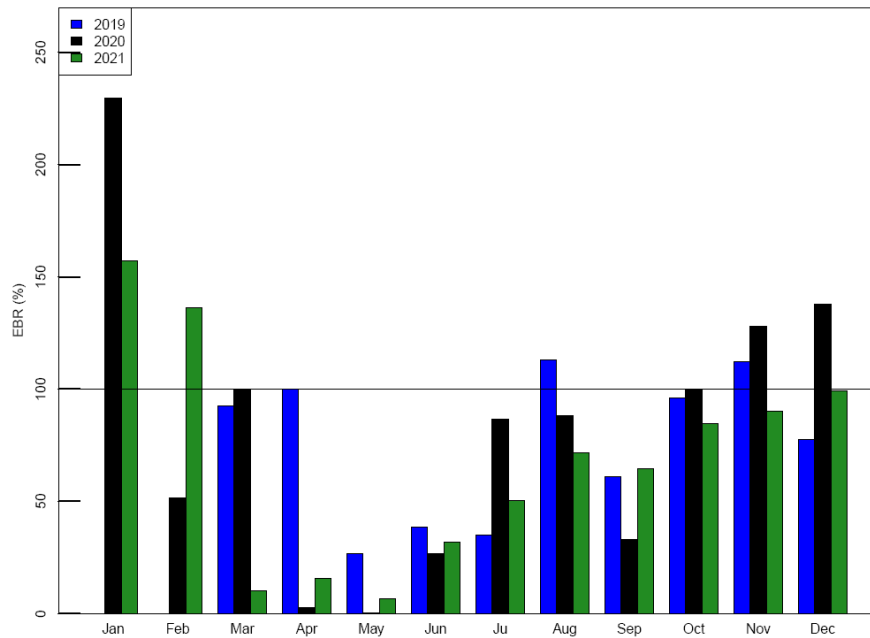


Figure 15: Monthly EBR from March 2019 to December 2021. Note that ΔHS were calculated over a 15-m

depth except for November and December 2020 and 2021, for which it was calculated for an h of 30-m and 44-m depths respectively.

Some uncertainties lie in the evaluation of ΔH_S . The monthly EBR was calculated using a ΔH_S for depths of 0-15 m, 0-30 m or 0-44 m, which correspond to the average depths of the thermocline for January to October, November and December, respectively. The water between the surface and these depths represent good approximations of heat storage in the water column. This is because the thermal mixing is spatially constrained by the thermocline. However, there is uncertainty in estimating these thermocline depths, which may lead to errors in the evaluation of ΔH_S .

Note that for 2019, there were no data for depths below 15 m. When we calculated ΔH_S for a 30-m and a 44-m depth, the EBR for November and December 2020 was 101% and 138% respectively. This was less than the 150% and 440% calculated for the water between the surface and 15-m depth.

4. CONCLUSION

This study quantified the temporal dynamics of evaporation over a deep, boreal, dimictic hydroelectric reservoir using two eddy-covariance setups, one mounted on a raft and one onshore. Data were collected for four years, from June 2018 to June 2022, in order to examine the daily, monthly and annual patterns of the turbulent heat fluxes.

Turbulent heat fluxes revealed opposite diurnal cycles of H and LE during heat storage and heat release periods, and the absence of a diurnal pattern during the rest of the year. LE reached its maximum at 15:00 when H reached its minimum, and LE was minimal at night at 00:00 while H peaked at 05:00 in the morning. Our monthly analysis showed that most of the latent and sensible heat fluxes occurred from August to December. The cumulative latent heat flux amounted to 84% of the annual evaporation. Three- and six-month delays occurred between maximum summer net radiation and maximum values of LE and H , respectively, suggesting the impact of the heat storage release. Moreover, one- and four-month delays were observed between the maximum surface water temperature and maximum LE and H , respectively.

Results showed an annual evaporation of $590 \pm 66 \text{ mm yr}^{-1}$ that was quite constant from year to year, with frequent 1-day to 2-day sustained events. Latent heat flux increased earlier than the sensible heat flux but also decreased before the sensible heat flux, resulting in a Bowen ratio that varied from a near-zero negative value in July to 1.5 in December. Vapour pressure-controlled evaporation induced a steady decline from September to December due to decreasing air temperature.

The large time lag and the magnitude of the energy storage within the water column made it difficult to close the energy balance. Therefore, in this study, we have taken that issue into account by correcting the annual cumulative evaporation while preserving of the measured Bowen ratio.

Moreover, monthly and seasonal patterns of evaporation can be related to the energy state of the reservoir. Indeed, depending on the time of year, the reservoir was either under ice cover or in heat storage or heat release conditions, which drives the magnitude of evaporation.

Results clearly illustrate that water loss through evaporation has a low impact on hydroelectricity production and water availability downstream. However, because evaporation is likely to increase in the region due to climate change, the assessment of this energy and the associated hydraulic components remains topical and essential to understanding future trends.

ACKNOWLEDGEMENTS

The authors would like to acknowledge Hydro-Québec for their collaboration, and more specifically François Bilodeau. They are also grateful to Annie-Claude Parent, Dany Crépault, Denis Jobin, Jaril Deschamps, Philippe Richard, Benjamin Bouchard, Habiba Kallel, Alexis Trottier-Paquet, and Gonzalo Leonardini Quelca for their help in field-related activities. This research was funded by the Natural Sciences and Engineering Research Council of Canada (NSERC) through grant RDCPJ508080-16 titled, “Observation and modelling of net evaporation from a boreal hydroelectric complex (water footprint)”.

DATA AVAILABILITY: Data available upon request.

REFERENCES

- Adrian, R., O'Reilly, C. M., Zagarese, H., Baines, S. B., Hessen, D. O., Keller, W., Livingstone, D. M., Sommaruga, R., Straile, D., Van Donk, E., Weyhenmeyer, G. A., & Winder, M. (2009). Lakes as sentinels of climate change. *Limnology and Oceanography*, *54* (6part2), 2283-2297. doi:https://doi.org/10.4319/lo.2009.54.6-part_2.2283
- Assouline, S., & Narkis, K. (2021). Reducing evaporation from water reservoirs using floating lattice structures. *Water Resources Research*, *57* (6), e2021WR029670. doi:<https://doi.org/10.1029/2021WR029670>
- Baldocchi, D. D., Hincks, B. B., & Meyers, T. P. (1988). Measuring biosphere-atmosphere exchanges of biologically related gases with micrometeorological methods. *Ecology*, *69* (5), 1331-1340. doi:<https://doi.org/10.2307/1941631>
- Beck, H. E., Zimmermann, N. E., McVicar, T. R., Vergopolan, N., Berg, A., & Wood, E. F. (2018). Present and future Köppen-Geiger climate classification maps at 1-km resolution. *Scientific Data*, *5* (1), 180214. doi:<https://doi.org/10.1038/sdata.2018.214>
- Blanken, P. D., Rouse, W. R., Culf, A. D., Spence, C., Boudreau, L. D., Jasper, J. N., Kochtubajda, B., Schertzer, W. M., Marsh, P., & Versegny, D. (2000). Eddy covariance measurements of evaporation from Great Slave Lake, Northwest Territories, Canada. *Water Resources Research*, *36* (4), 1069-1077. doi:<https://doi.org/10.1029/1999WR900338>
- Blanken, P. D., Spence, C., Hedstrom, N., & Lenters, J. D. (2011). Evaporation from Lake Superior: 1. Physical controls and processes. *Journal of Great Lakes Research*, *37* (4), 707-716. doi:<https://doi.org/10.1016/j.jglr.2011.08.009>
- Cole, G. A., & Weihe, P. E. (2016). *Textbook of limnology* (5th ed.). Prospect Heights, Ill.: Waveland Press.
- Downing, J. A., Prairie, Y. T., Cole, J. J., Duarte, C. M., Tranvik, L. J., Striegl, R. G., McDowell, W. H., Kortelainen, P., Caraco, N. F., Melack, J. M., & Middelburg, J. J. (2006). The global abundance and size distribution of lakes, ponds, and impoundments. *Limnology and Oceanography*, *51* (5), 2388-2397. doi:<https://doi.org/10.4319/lo.2006.51.5.2388>
- Feng, J. W., Liu, H. Z., Sun, J. H., & Wang, L. (2016). The surface energy budget and interannual variation of the annual total evaporation over a highland lake in Southwest China. *Theoretical and Applied Climatology*, *126* (1-2), 303-312. doi:<https://doi.org/10.1007/s00704-015-1585-9>
- Finkelstein, P. L., & Sims, P. F. (2001). Sampling error in eddy correlation flux measurements. *Journal of Geophysical Research: Atmospheres*, *106* (D4), 3503-3509. doi:<https://doi.org/10.1029/2000JD900731>
- Foken, T. (2008). The energy balance closure problem: An overview. *Ecological Applications*, *18* (6), 1351-1367. doi:<http://doi.org/10.1890/06-0922.1>
- Fournier, J., Thibault, A., Nadeau, D. F., Vercauteren, N., Anctil, F., Parent, A.-C., Strachan, I. B., & Tremblay, A. (2021). Evaporation from boreal reservoirs: A comparison between eddy covariance observations and estimates relying on limited data. *Hydrological Processes*, *35* (8), e14335. doi:<https://doi.org/10.1002/hyp.14335>
- Friedrich, K., Grossman, R. L., Huntington, J., Blanken, P. D., Lenters, J., Holman, K. D., Gochis, D., Livneh, B., Prairie, J., Skeie, E., Healey, N. C., Dahm, K., Pearson, C., Fennessey, T., Hook, S. J., & Kowalski, T. (2018). Reservoir evaporation in the Western United States. *Bulletin of the American Meteorological Society*, *99* (1), 167-187. doi:<http://doi.org/10.1175/BAMS-D-15-00224.1>
- Gorham, E. (1964). Morphometric Control of annual heat budgets in temperate lakes. *Limnology and Oceanography*, *9* (4), 525-529. doi:<https://doi.org/10.4319/lo.1964.9.4.0525>

- Heikinheimo, M., Kangas, M., Tourula, T., Venäläinen, A., & Tattari, S. (1999). Momentum and heat fluxes over lakes Tännaren and Råksjö determined by the bulk-aerodynamic and eddy-correlation methods. *Agricultural and Forest Meteorology*, *98-99* , 521-534. doi:[https://doi.org/10.1016/S0168-1923\(99\)00121-5](https://doi.org/10.1016/S0168-1923(99)00121-5)
- Hydro-Québec. (2007). *Complexe de la Romaine – Étude d'impact sur l'environnement* . In Vol. 1 : Vue d'ensemble et description des aménagements. (pp. 314). Retrieved from <https://www.hydroquebec.com/romaine/documents/etude.html>
- Koenings, J. P., & Edmundson, J. A. (1991). Secchi disk and photometer estimates of light regimes in Alaskan lakes: Effects of yellow color and turbidity. *Limnology and Oceanography*, *36* (1), 91-105. doi:<https://doi.org/10.4319/lo.1991.36.1.0091>
- Laird, N. F., & Kristovich, D. A. R. (2002). Variations of sensible and latent heat fluxes from a great lakes buoy and associated synoptic weather patterns. *Journal of Hydrometeorology*, *3* (1), 3-12. doi:[https://doi.org/10.1175/1525-7541\(2002\)003%3C0003:VOSALH%3E2.0.CO;2](https://doi.org/10.1175/1525-7541(2002)003%3C0003:VOSALH%3E2.0.CO;2)
- Lensky, N. G., Lensky, I. M., Peretz, A., Gertman, I., Tanny, J., & Assouline, S. (2018). Diurnal course of evaporation from the dead sea in summer: A distinct double peak induced by solar radiation and night sea breeze. *Water Resources Research*, *54* (1), 150-160. doi:<https://doi.org/10.1002/2017WR021536>
- Markfort, C. D., Perez, A. L. S., Thill, J. W., Jaster, D. A., Porte-Agel, F., & Stefan, H. G. (2010). Wind sheltering of a lake by a tree canopy or bluff topography. *Water Resources Research*, *46* (3). doi:<https://doi.org/10.1029/2009WR007759>
- Mauder, M., Cuntz, M., Drüe, C., Graf, A., Rebmann, C., Schmid, H. P., Schmidt, M., & Steinbrecher, R. (2013). A strategy for quality and uncertainty assessment of long-term eddy-covariance measurements. *Agricultural and Forest Meteorology*, *169* , 122-135. doi:<http://doi.org/10.1016/j.agrformet.2012.09.006>
- Mauder, M., & Foken, T. (2011). *Documentation and instruction manual of the Eddy-Covariance Software package TK3* . Bayreuth: Univ., Abt. Mikrometeorologie.
- Mauder, M., Genzel, S., Fu, J., Kiese, R., Soltani, M., Steinbrecher, R., Zeeman, M., Banerjee, T., De Roo, F., & Kunstmann, H. (2018). Evaluation of energy balance closure adjustment methods by independent evapotranspiration estimates from lysimeters and hydrological simulations. *Hydrological Processes*, *32* (1), 39-50. doi:<http://doi.org/10.1002/hyp.11397>
- McJannet, D., Hawdon, A., Van Niel, T., Boadle, D., Baker, B., Trefry, M., & Rea, I. (2017). Measurements of evaporation from a mine void lake and testing of modelling approaches. *Journal of Hydrology*, *555* , 631-647. doi:<https://doi.org/10.1016/j.jhydrol.2017.10.064>
- Miller, S. D., Hristov, T., Edson, J., & Friehe, C. (2008). Platform motion effects on measurements of turbulence and air-sea exchange over the open ocean. *Journal of Atmospheric and Oceanic Technology*, *25* (9), 1683-1694. doi:<https://doi.org/10.1175/2008JTECHO547.1>
- Nordbo, A., Launiainen, S., Mammarella, I., Lepparanta, M., Huotari, J., Ojala, A., & Vesala, T. (2011). Long-term energy flux measurements and energy balance over a small boreal lake using eddy covariance technique. *Journal of Geophysical Research - Part D - Atmospheres*, *116* (D2), D02119 (02117 pp.). doi:<https://doi.org/10.1029/2010JD014542>
- Papale, D., Reichstein, M., Aubinet, M., Canfora, E., Bernhofer, C., Kutsch, W., Longdoz, B., Rambal, S., Valentini, R., Vesala, T., & Yakir, D. (2006). Towards a standardized processing of Net Ecosystem Exchange measured with eddy covariance technique: algorithms and uncertainty estimation. *Biogeosciences*, *3* (4), 571-583. doi:<https://doi.org/10.5194/bg-3-571-2006>
- Patel, S., & Rix, A. (2019). *Water surface albedo modelling for floating PV plants* . Paper presented at the 6th Southern African Solar Energy Conference (SASEC), Port Alfred, South Africa.

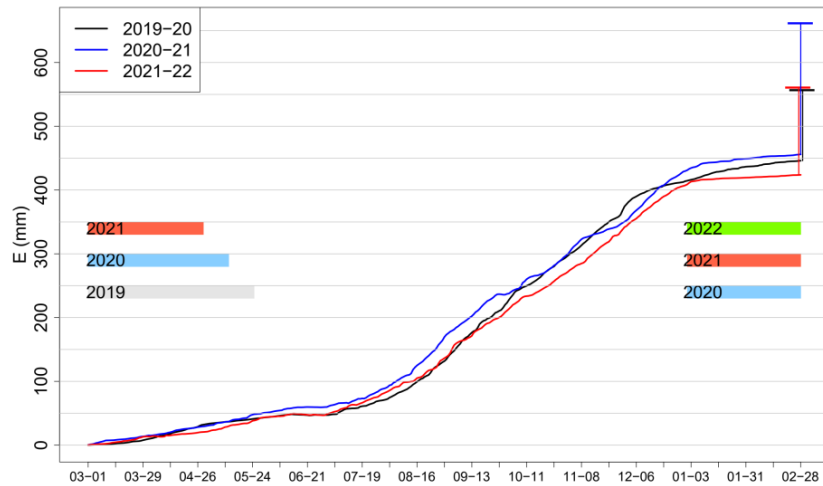
- Pérez, A., Lagos, O., Lillo-Saavedra, M., Souto, C., Paredes, J., & Arumí, J. L. (2020). Mountain Lake Evaporation: A Comparative Study between Hourly Estimations Models and In Situ Measurements. *Water*, *12* (9), 2648. doi:<https://doi.org/doi:10.3390/w12092648>
- Piccolroaz, S., Toffolon, M., & Majone, B. (2015). The role of stratification on lakes' thermal response: The case of Lake Superior. *Water Resources Research*, *51* (10), 7878-7894. doi:<https://doi.org/10.1002/2014WR016555>
- Pierre, A., Isabelle, P.-E., Nadeau, D. F., Thiboult, A., Perelet, A. O., Rousseau, A. N., Anctil, F., & Deschamps, J. (2022). Estimating Sensible and Latent Heat Fluxes over an Inland Water Body Using Optical and Microwave Scintillometers. *Boundary-Layer Meteorology* . doi:<https://doi.org/10.1007/s10546-022-00732-7>
- Reichstein, M., Falge, E., Baldocchi, D., Papale, D., Aubinet, M., Berbigier, P., Bernhofer, C., Buchmann, N., Gilmanov, T., Granier, A., Grünwald, T., Havránková, K., Ilvesniemi, H., Janous, D., Knohl, A., Laurila, T., Lohila, A., Loustau, D., Matteucci, G., Meyers, T., Miglietta, F., Ourcival, J.-M., Pumpanen, J., Rambal, S., Rotenberg, E., Sanz, M., Tenhunen, J., Seufert, G., Vaccari, F., Vesala, T., Yakir, D., & Valentini, R. (2005). On the separation of net ecosystem exchange into assimilation and ecosystem respiration: review and improved algorithm. *Global Change Biology*, *11* (9), 1424-1439. doi:<https://doi.org/10.1111/j.1365-2486.2005.001002.x>
- Rouse, W. R., Oswald, C. M., Binyamin, J., Blanken, P. D., Schertzer, W. M., & Spence, C. (2003). Interannual and seasonal variability of the surface energy balance and temperature of central Great Slave Lake. *Journal of Hydrometeorology*, *4* (4), 720-730. doi:10.1175/1525-7541(2003)004<0720:IASVOT>2.0.CO;2
- Spence, C., Blanken, P. D., Lenters, J. D., & Hedstrom, N. (2013). The Importance of Spring and Autumn Atmospheric Conditions for the Evaporation Regime of Lake Superior. *Journal of Hydrometeorology*, *14* (5), 1647-1658. doi:<https://doi.org/10.1175/JHM-D-12-0170.1>
- Spence, C., Rouse, W. R., Worth, D., & Oswald, C. (2003). Energy budget processes of a small Northern Lake. *Journal of Hydrometeorology*, *4* (4), 694-701. doi:10.1175/1525-7541(2003)004<0694:EBPOAS>2.0.CO;2
- Strachan, I. B., Tremblay, A., Pelletier, L., Tardif, S., Turpin, C., & Nugent, K. A. (2016). Does the creation of a boreal hydroelectric reservoir result in a net change in evaporation? *Journal of Hydrology*, *540* , 886-899. doi:<https://doi.org/10.1016/j.jhydrol.2016.06.067>
- Tanny, J., Cohen, S., Assouline, S., Lange, F., Grava, A., Berger, D., Teltch, B., & Parlange, M. B. (2008). Evaporation from a small water reservoir: Direct measurements and estimates. *Journal of Hydrology*, *351* (1-2), 218-229. doi:<https://doi.org/10.1016/j.jhydrol.2007.12.012>
- Venäläinen, A., Heikinheimo, M., & Tourula, T. (1998). Latent heat flux from small sheltered lakes. *Boundary-Layer Meteorology*, *86* (3), 355-377. doi:<https://doi.org/10.1023/A:1000664615657>
- Vickers, D., & Mahrt, L. (1997). Quality control and flux sampling problems for tower and aircraft data. *Journal of Atmospheric and Oceanic Technology*, *14* (3), 512-526. doi:10.1175/1520-0426(1997)014<0512:QCAFSP>2.0.CO;2
- Vincent, W. F. (2018). *Lakes – A very short introduction* . In (pp. 160).
- Wang, W., Lee, X., Xiao, W., Liu, S., Wang, Y., Zhang, M., Zhao, L., & Schultz, N. (2018). Global lake evaporation accelerated by changes in surface energy allocation in a warmer climate. *Nature Geoscience*, *11* (6), 410-414. doi:<https://doi.org/10.1038/s41561-018-0114-8>
- Wang, W., Roulet, N. T., Strachan, I. B., & Tremblay, A. (2016). Modeling surface energy fluxes and thermal dynamics of a seasonally ice-covered hydroelectric reservoir. *Science of the Total Environment*, *550* , 793-805. doi:<https://doi.org/10.1016/j.scitotenv.2016.01.101>

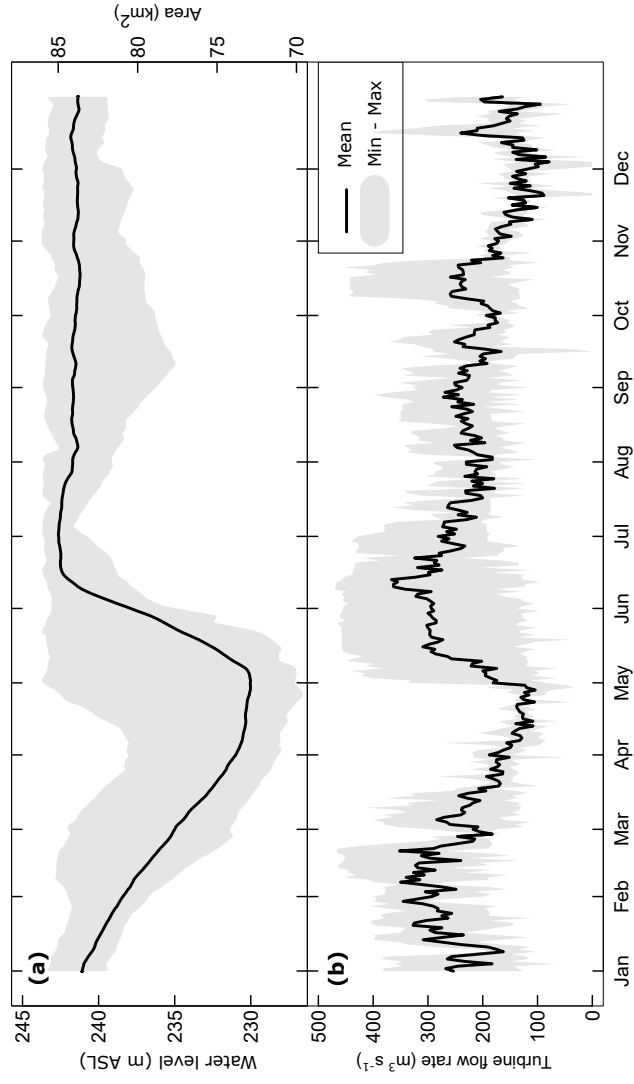
Webb, E. K., Pearman, G. I., & Leuning, R. (1980). Correction of flux measurements for density effects due to heat and water vapour transfer. *Quarterly Journal of the Royal Meteorological Society*, 106 (447), 85-100. doi:<https://doi.org/10.1002/qj.49710644707>

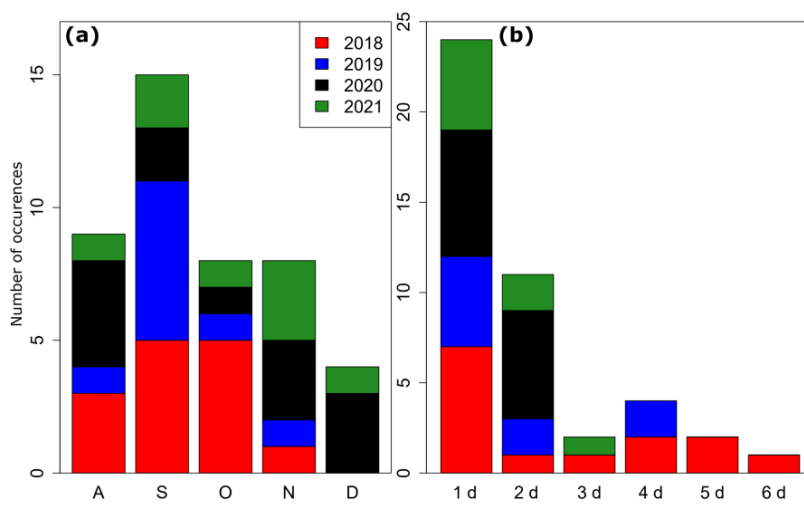
Wilczak, J. M., Oncley, S. P., & Stage, S. A. (2001). Sonic anemometer tilt correction algorithms. *Boundary-Layer Meteorology*, 99 (1), 127-150. doi:<https://doi.org/10.1023/A:1018966204465>

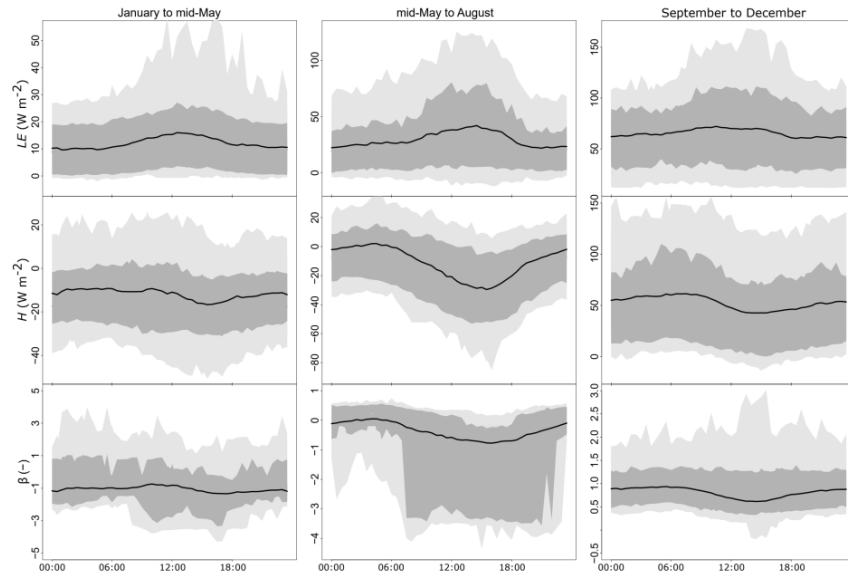
Williamson, C. E., Saros, J. E., & Schindler, D. W. (2009). Climate change: Sentinels of change. *Science*, 323 (5916), 887-888. doi:<https://doi.org/10.1126/science.1169443>

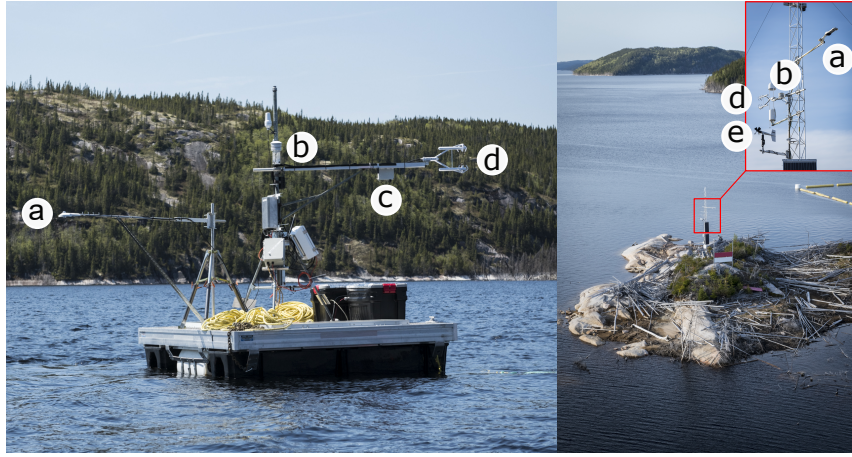
Williamson, C. E., Saros, J. E., Vincent, W. F., & Smol, J. P. (2009). Lakes and reservoirs as sentinels, integrators, and regulators of climate change. *Limnology and Oceanography*, 54 (6part2), 2273-2282. doi:https://doi.org/10.4319/lo.2009.54.6-part_2.2273

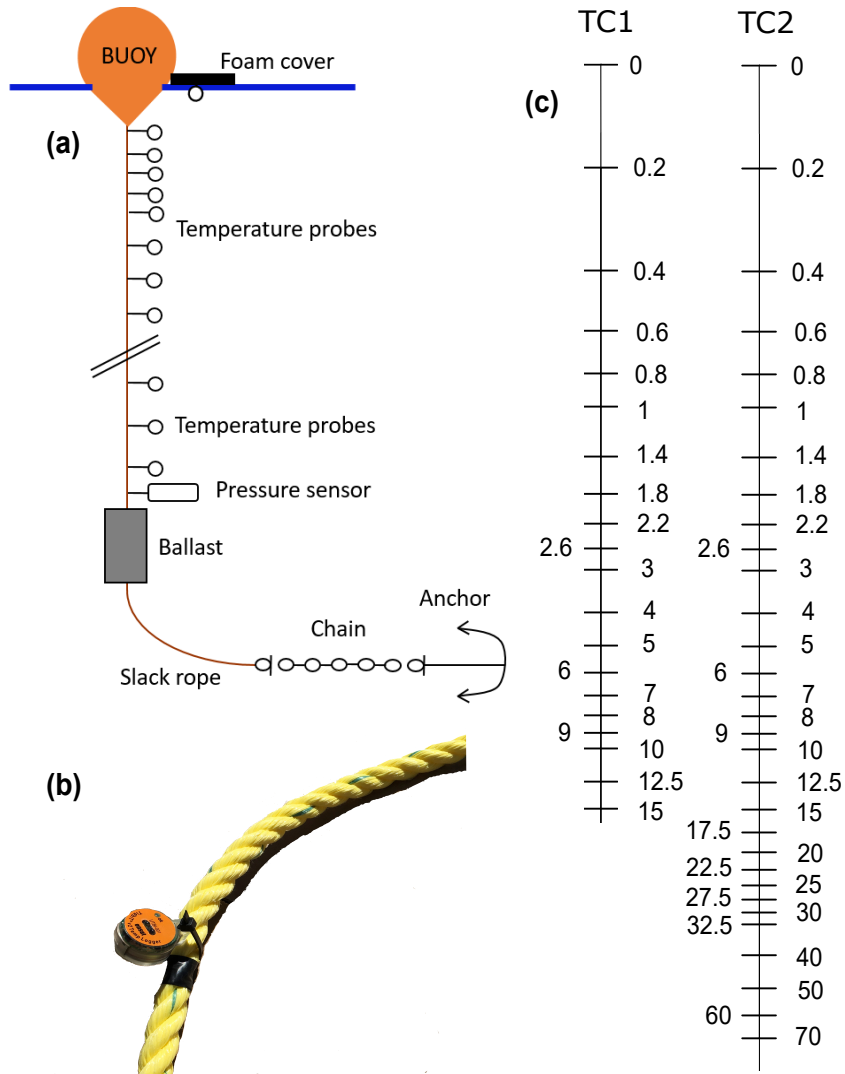


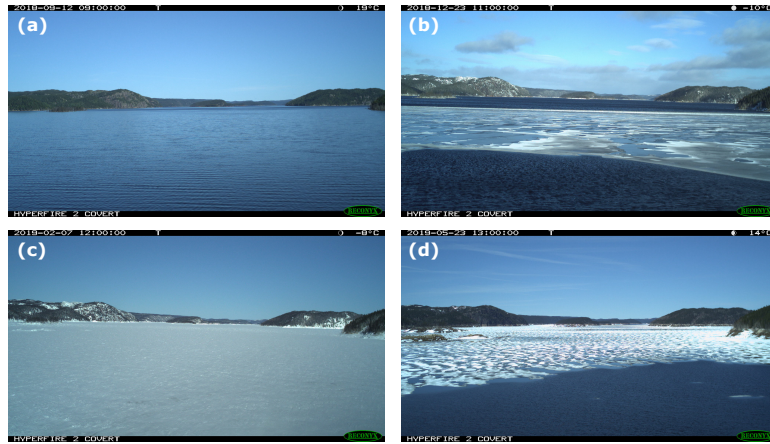


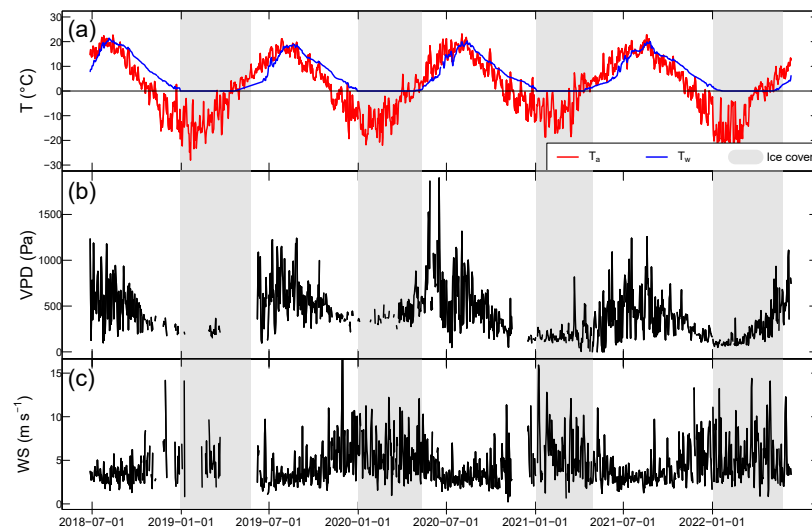


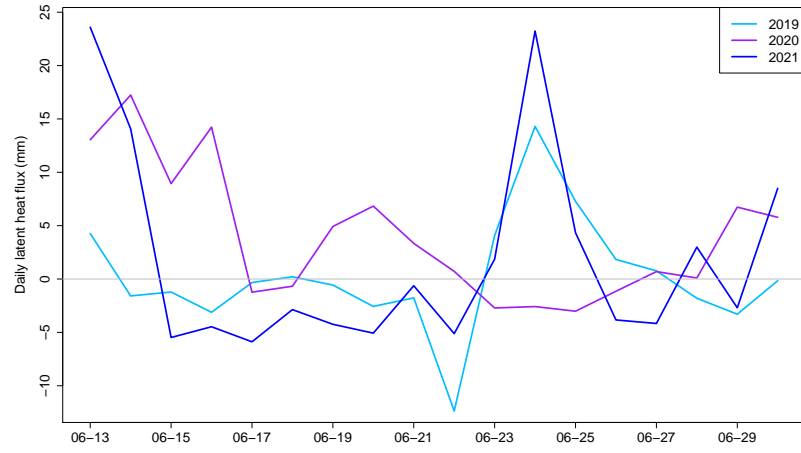


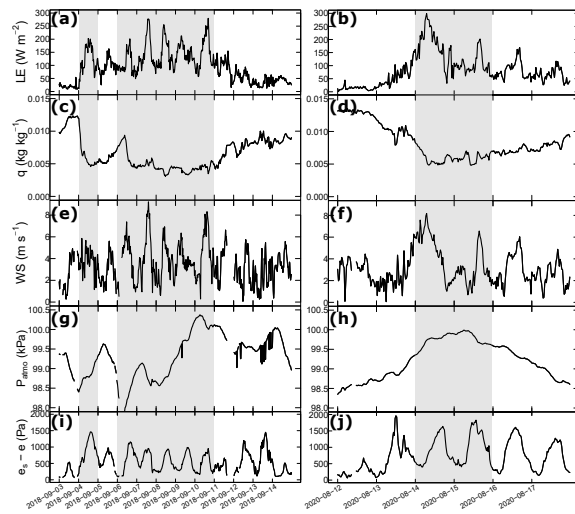


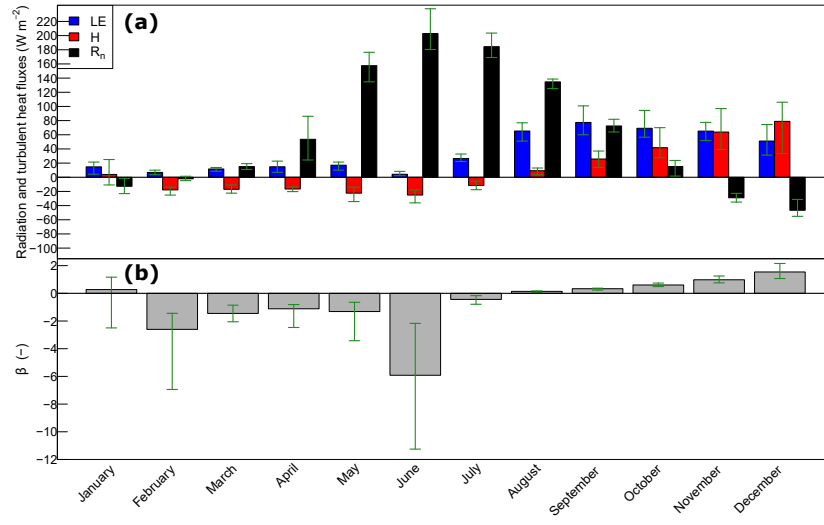


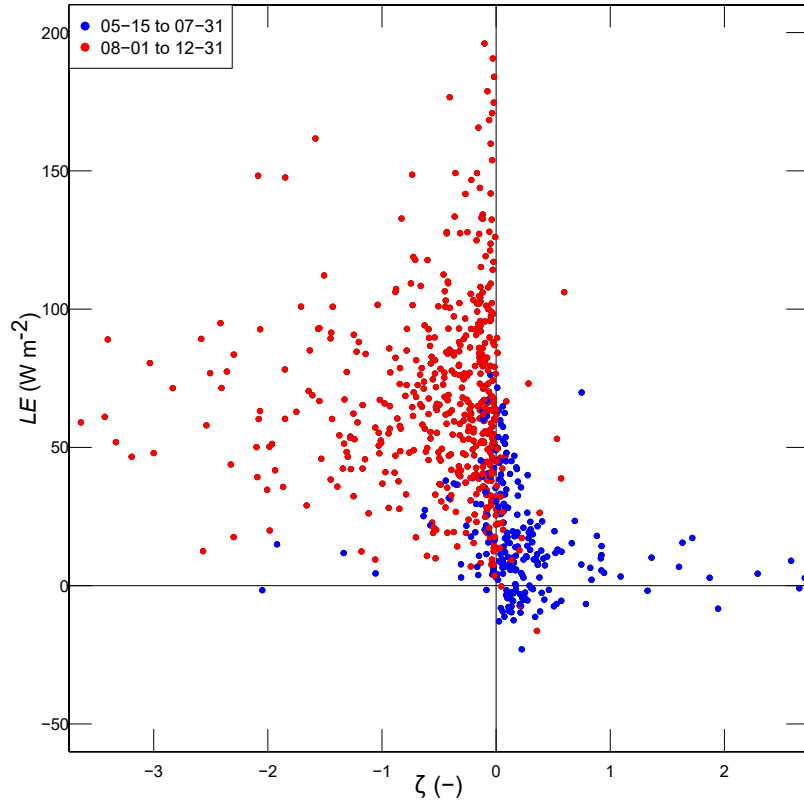


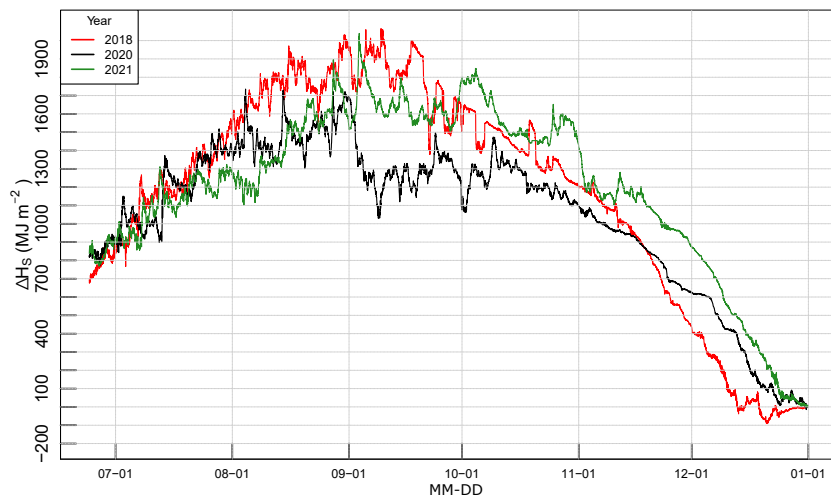


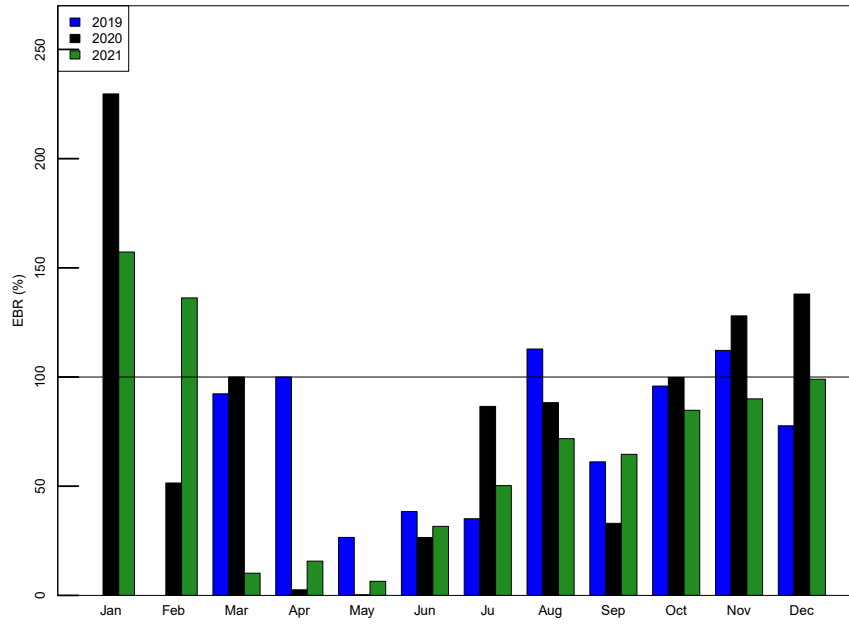


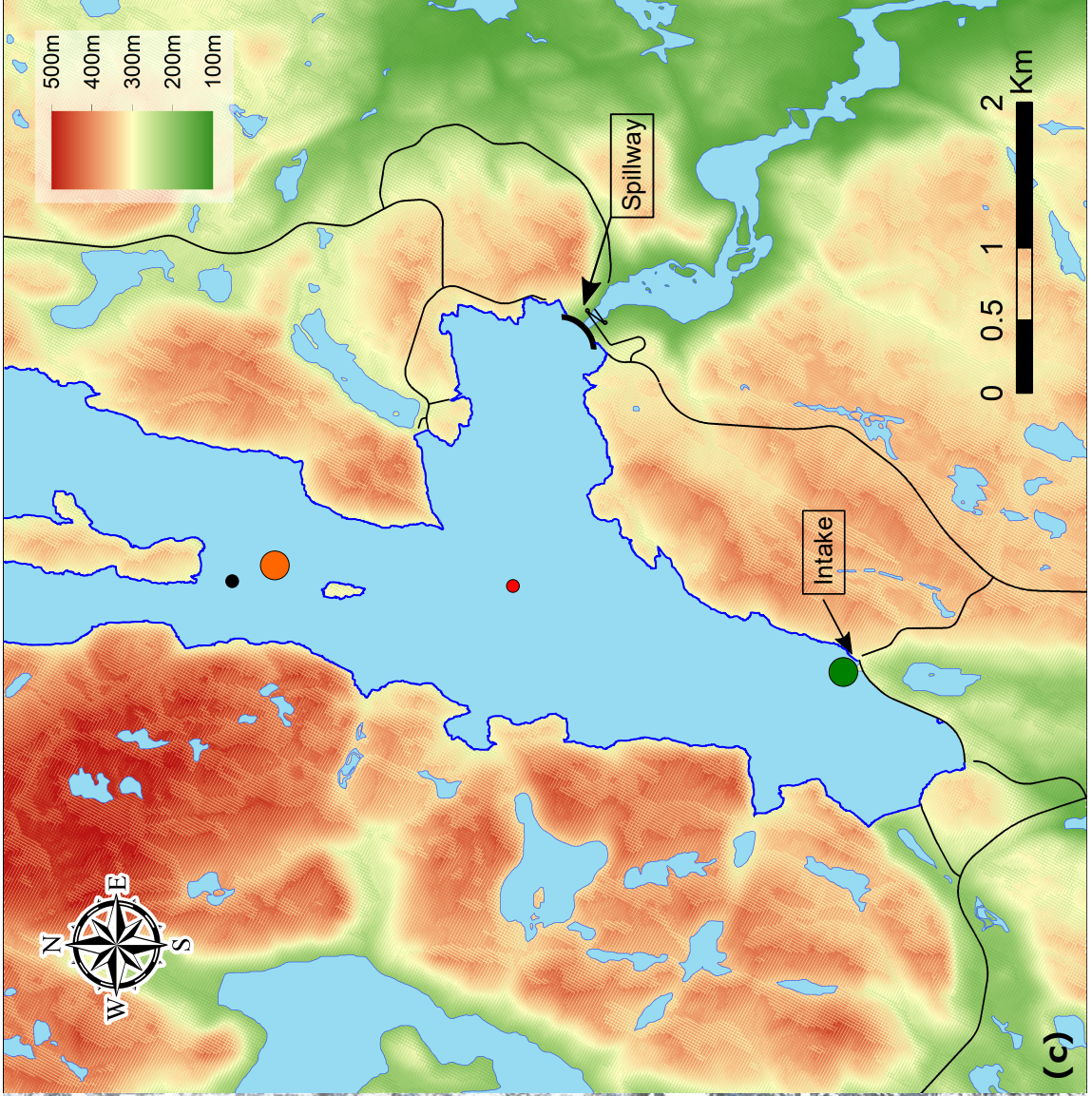
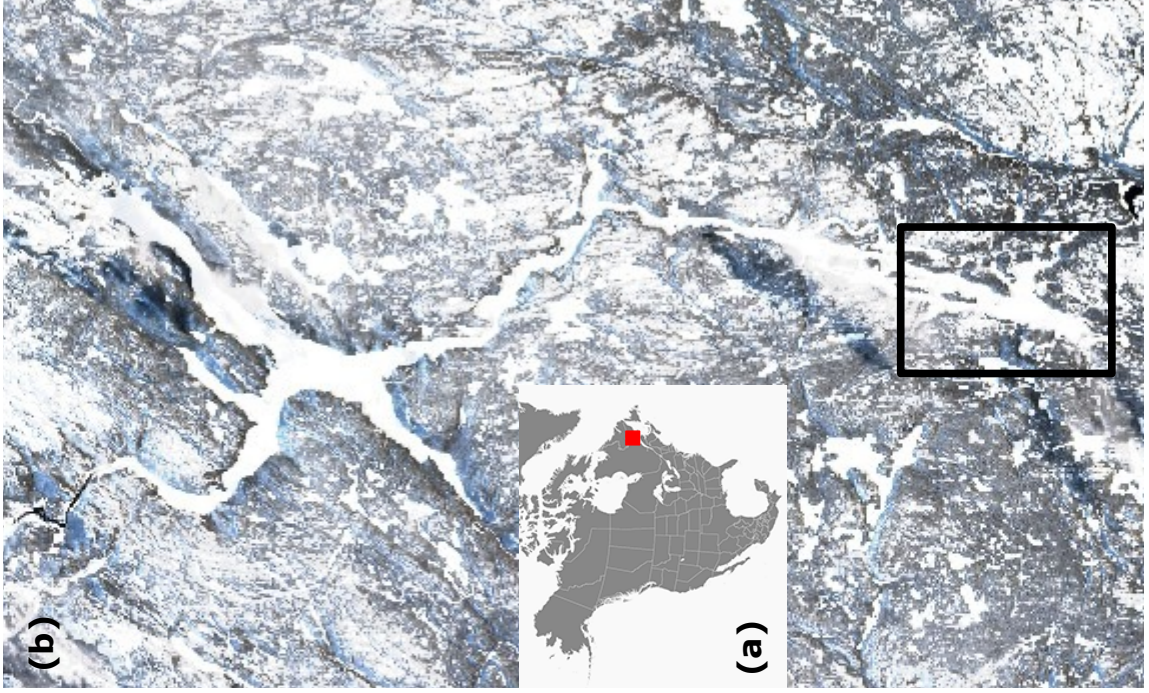












- Raft Flux Tower
- Shore Flux Tower
- TC1
- TC2